

## Coalescence of liquid drops by surface tension

A. Menchaca-Rocha, A. Martínez-Dávalos, and R. Núñez

*Instituto de Física, Universidad Nacional Autónoma de México, Apartado Postal 20-364, 01000 México Distrito Federal, México*

S. Popinet and S. Zaleski

*Modélisation en Mécanique, CNRS UMR 7607, Université Pierre et Marie Curie, 8 rue du Capitaine Scott, 75015 Paris, France*

(Received 6 November 2000; published 27 March 2001)

The merging of two mercury drops at very low kinetic energy is observed using fast, digital, and analog imaging techniques. Sequences showing the time evolution of the overall-surface shape as well as an amplified view of the contact region are shown. Qualitative and quantitative comparisons with computations of the Navier-Stokes equation with a free surface are made. In the model, the surface is tracked by a marker-chain method.

DOI: 10.1103/PhysRevE.63.046309

PACS number(s): 47.55.Dz, 47.20.Dr, 47.11.+j, 47.80.+v

### I. INTRODUCTION

Consider the surface-shape evolution of two liquid drops put in contact at such low relative velocity ( $V_r$ ) that surface-tension effects dominate over initial kinetic-energy perturbations. In those conditions, once the interface separating the fluid masses ruptures, the excess surface-energy induces an unstable situation driving the system towards its new equilibrium (spherical) shape. Expected to be of a general nature [1], and relevant to a wide variety of fields, ranging from low-energy fusion of atomic nuclei [2] and molecular clusters [3] to rain-drop formation in clouds [4], so far this phenomenon remained largely unexplored. Here we report on observations involving the coalescence of mercury drops lying on a horizontal glass surface, specially treated [5] to minimize wetting effects. Our comparison with numeric calculations for free liquid drops shows a good overall agreement, allowing a deeper insight into the dynamics of the interaction.

### II. EXPERIMENT

The experimental difficulty involved in this type of studies consists in producing liquid drops moving freely against each other at a negligible small relative velocity, assuring that the coalescence action occurs within the focal plane of a high-resolution imaging device. In an earthly laboratory environment, important problems arise when trying to keep in focus the magnified image of free falling drops. The use of dynamic levitators (magnetic, acoustic, gas jets, etc.) to tackle this problem introduces undesirable initial surface oscillations, while the corresponding fields, being affected by close-focusing devices (such as microscope lenses) become highly unstable. Thus, we chose the simpler approach of observing the coalescence of mercury drops, having masses  $m$  in the 0.1–1.5-g range, by placing them on an optimized roughous, horizontal, glass surface. The roughening procedure, described in detail elsewhere [5], results in a fivefold gain in the mobility of the mercury drops. Due to the large effective contact angle obtained ( $\approx 160^\circ$ ) small mercury drops adopt near-spherical shapes. Hence, axial symmetry produces close similarities between a vertical projection of

the coalescence between our slightly deformed drops and two-dimensional (2D) projections of the actual 3D (free drops) case. With those limitations, our technique presents the main advantage of allowing to fix the center of mass of the two-drop system in the laboratory frame of reference, while minimizing initial drop perturbations.

The action was recorded with both, a fast-digital camera [6] capable of taking up to 830 frames per second (fps) and an ultrafast analog camera [7] that can take from  $5 \times 10^4$  fps to  $10^6$  fps. When using the fast-digital camera, the field of view comprised the whole two-drop system, as schematically illustrated in Fig. 1. In the case of the ultrafast camera, the action was observed through a microscope using a  $\times 10$  magnification lens as indicated in Fig. 2. It is worth noting that the focal distance of those lenses is a decreasing function of their magnifying power, but their transverse dimension remains approximately constant, hence the use of larger magnification factors is prevented by the height of the drops.

In the setup of Fig. 1, the initial contact between two mercury ( $\rho = 13\,600 \text{ kg/m}^3$ ) drops is induced by placing one of them on the glass surface, while slowly ( $V_r \leq 1 \text{ mm/s}$ ) approaching the second one with the aid of a thin (0.1 mm) plastic sheet sliding along (and parallel to) the glass. The corresponding kinetic energy  $E_k$  is three orders of magnitude smaller than the excess surface energy  $\Delta E_s = (2 - 2^{2/3})S\sigma$ , where  $\sigma$  is the surface-tension coefficient ( $0.435 \text{ J/m}^2$  for mercury), and  $S = 4\pi r^2$ ,  $r$  being the drops' radii. In this

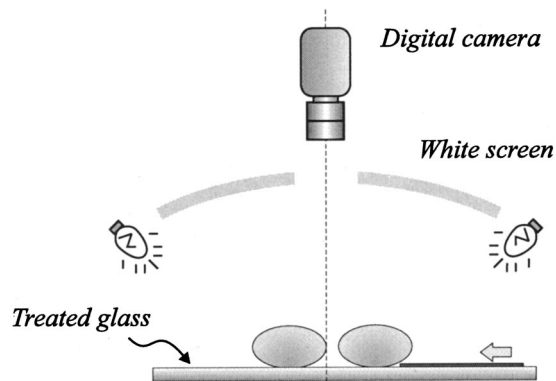


FIG. 1. Fast digital camera setup used to obtain an overall view.

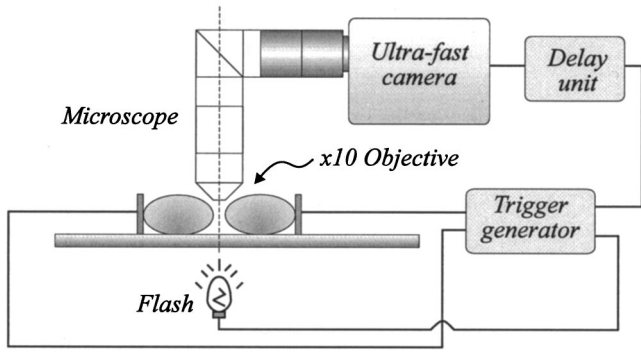


FIG. 2. Ultrafast analog camera setup used to obtain a magnified view of the contact region (see arrow in Fig. 3).

experimental arrangement, the action was illuminated from above, using a white screen with a small hole in the middle to allow for the camera’s lens. These produced images looking like hollow shiny discs, as shown in the sequence of Fig. 3. A close resemblance between this figure and images reported by Park and Crosby [8] of collisions between free-falling water drops (see their Fig. 7), although taken at higher kinetic energy ( $E_k \approx 10\Delta E_s$ ), supports our choice of experimental arrangement.

In the setup shown in Fig. 2, aimed at studying earlier stages, the magnified images were restricted to one-half of the contact region (arrow in Fig. 3), as shown in the sequence of Fig. 4. In this case the mercury drops were slowly (again,  $V_r \leq 1$  mm/s) approached against each other using concave stainless steel electrodes, which, through a small electric potential (10 mV), also served to generate a rapid ( $\leq 1 \mu\text{s}$ ) electric pulse when the contact between the mercury surfaces was established. This signal was used to trigger a rapid ( $\leq 12\text{-}\mu\text{s}$  rise-time) flashlight and,  $10 \mu\text{s}$  later, the ultrafast camera. The reduced illumination in the 1st frame of Fig. 4 indicates that the light pulse is still  $2 \mu\text{s}$  away from the 1 ms-wide light-output plateau.

Although comprehensive understanding of the phenomenon requires observations during a time  $t_T$  spanning the whole oscillatory pattern, from first contact to complete damping, important information can be obtained during the time  $t_i$  taken by the initial perturbation to propagate from the contact region to the far end of the drops, as shown in Fig. 3, and during the first, neck-formation, instants (Fig. 4).

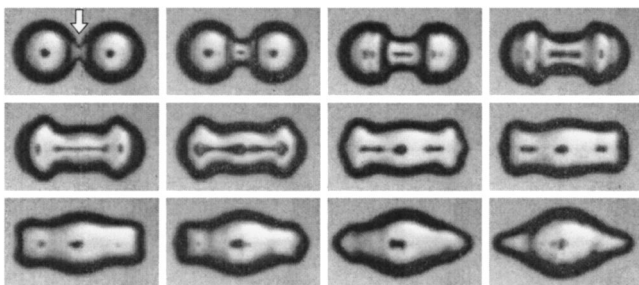


FIG. 3. Experimentally observed surface shape evolution of two 1.0-g mercury drops. Time runs from left to right, and from top to bottom. The time lapsed between images is  $\Delta t = 3.5$  ms. The sequence stops near the maximum horizontal stretching.

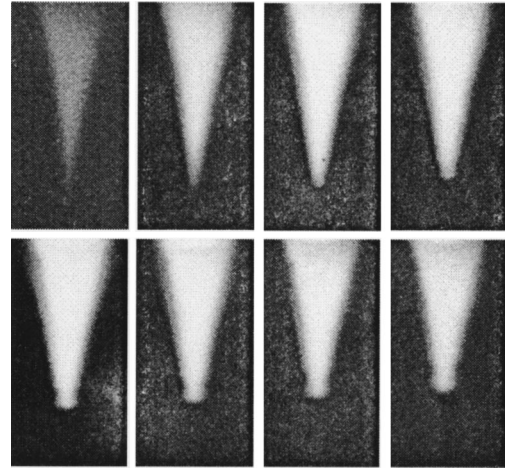


FIG. 4. Magnified evolution of the contact region, using the ultrafast-analog camera, with  $\Delta t = 20 \mu\text{s}$ . The first image was taken  $10 \mu\text{s}$  after electric contact between the drops was established. Other conventions as in Fig. 3.

### III. RESULTS

The sequence in Fig. 3, corresponding to  $m = 1$  g drops, shows the formation of a narrow cylindrical neck, preceded by large axial waves that propagate toward the undisturbed far ends. When those perturbations approach the extremes, the neck region bulges smoothly as the outer ends stretch out and, then, collapse (not shown), initiating a damping-oscillatory pattern. Using a Cartesian coordinate system, with its origin in the center of mass of the system (see Fig. 5) this behavior can be quantified by measuring the time evolution of two characteristic dimensions: the transverse  $R_y$  and axial  $R_x$  radii. For  $m = 1$  g drops, this result is illustrated in Figs. 6 and 7. Note how the initial contact ( $t = 0$ ) shows an immediate effect on  $R_y$ , initiating a monotonic increase, while on  $R_x$  an oscillatory behavior is observed only after some delay ( $t_i$  in Fig. 7), which eventually produces a maximum stretching  $R_{x,max}$ , at  $t_i$ . The time  $t_i$  is plotted in Fig. 8 as a function of  $m$ , where we observe a monotonically increasing function.

Concerning earlier stages, for  $m = 1$  g drops, Fig. 4 shows how the action evolves as a moving meniscus formed by the closing gap separating the mercury walls. Maximum illumi-

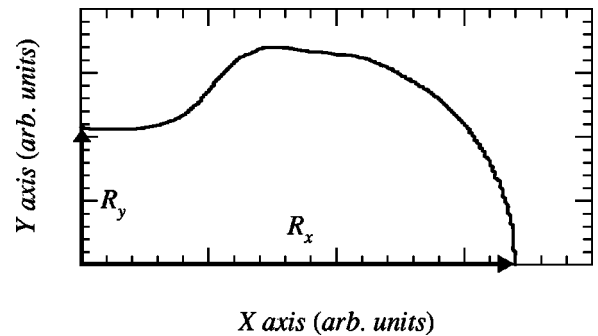


FIG. 5. Definition of transverse and axial radii,  $R_y$  and  $R_x$ , respectively. The curve shown as example is the digitized profile of the upper-right quadrant of the  $t = 10.5$  ms (third) frame in Fig. 3.

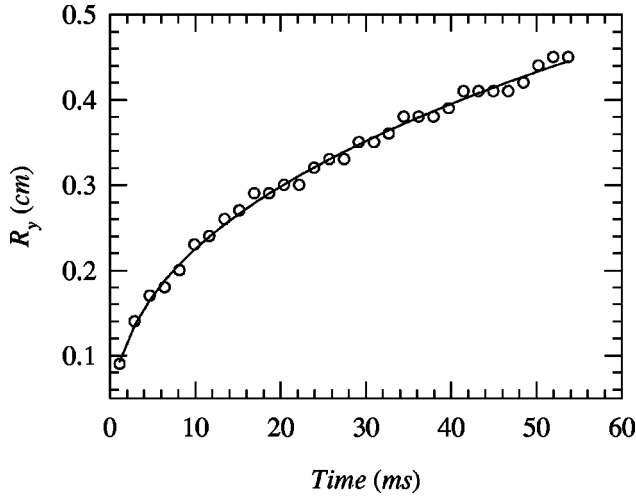


FIG. 6. Time evolution of  $R_y$ , measured in the coalescence for  $m=1$  g mercury drops using the fast camera. The continuous line represents the best fit to the data using a  $t^A$  law, yielding  $A=0.41$ .

nation in frame 3 ( $30 \mu\text{s}$  after trigger) allows a reliable  $R_y$  determination of  $\approx 200 \mu\text{m}$  (3% of the final diameter), which increases monotonically thereafter. The last four frames also show the appearance of a distinct rounded-up tip, as well as signs of the preceding capillary waves.

The  $R_y$  values extracted from Fig. 4 are plotted as a function of time in Fig. 9 (full circles). For comparison, we also reproduce the  $R_y$  values extracted from Fig. 3 (open circles). Note the small initial neck-growth rate, which we associate with the abrupt topological change occurring during the initial contact. Before interface rupture, the separated walls are perpendicular to the line joining the center of the drops (our  $x$  axis). Later stages show the walls joined by a near cylindrical neck, parallel to the  $x$  axis. Due to surface tension, this topological change tends to separate the walls, allowing sufficient light to reach the camera from smaller  $R_y$  regions, otherwise too close for that. Hence it is only when the rounded up tip (third frame in Fig. 4) becomes apparent that

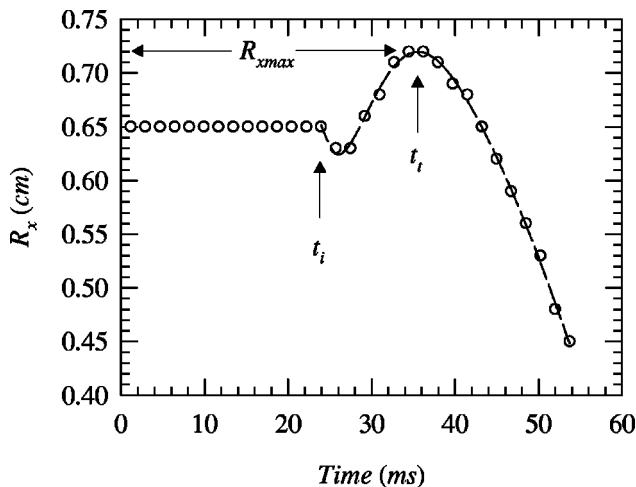


FIG. 7. Time evolution of  $R_x$ , measured in the coalescence for  $m=1$  g mercury drops using the fast camera, and definitions of  $t_i$ ,  $t_i$ , and  $R_{x\text{max}}$ . The dashed line is used to guide the eye.

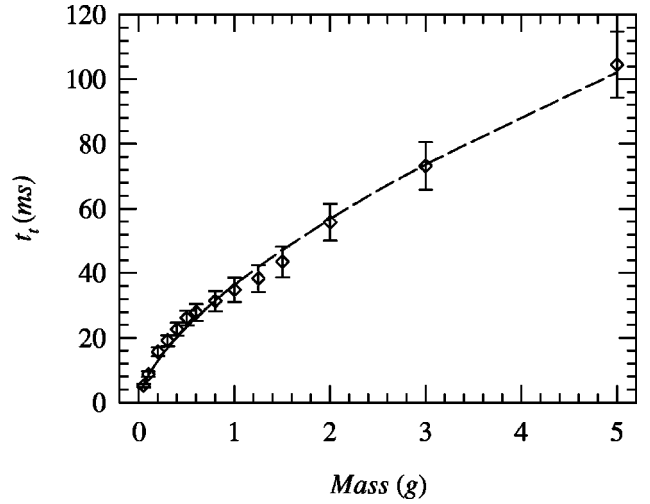


FIG. 8. Mass dependence of  $t_i$ . The dashed line is used to guide the eye.

we feel confident about the  $R_y$  measurements of Fig. 9 to represent the actual neck sizes. Using a  $R_y \propto t^A$  power law to fit the fast data of Fig. 6 (continuous line), a neck-growth rate value of  $A=0.41$  is obtained. As shown in Fig. 9, this growth rate joins smoothly with the ultrafast data (full circles), although the corresponding power-law fit (not shown) yields a higher slope of  $A=0.55$ , which is close to the recent  $A=0.5$  predictions of Eggers *et al.* [9] for the early stages.

#### IV. NUMERICAL SIMULATION

A numerical study was performed using the free-surface Navier-Stokes code developed at the Laboratoire de Modélisation en Mécanique, Paris. The Navier-Stokes equation for

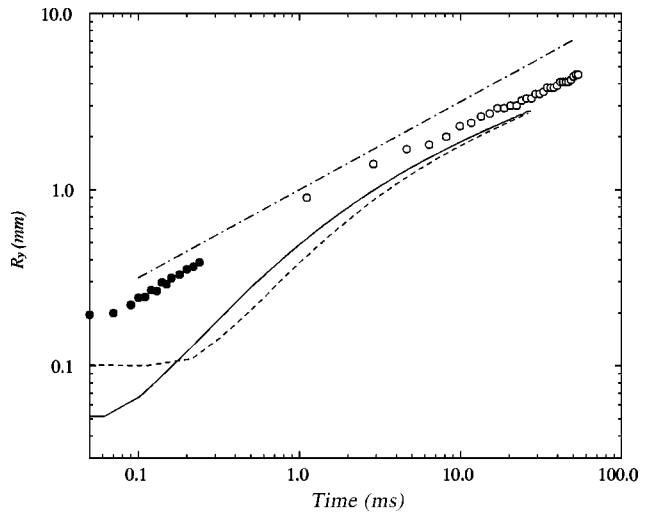


FIG. 9. The measured (circles) overall time evolution of  $R_y$  for  $m=1$  g mercury drops, including data taken with the ultrafast camera (full circles), is compared with numerical simulation predictions using two different grid sizes:  $512 \times 128$  (dashed line) and  $1024 \times 256$  (continuous line). The dot-dashed curve represents a  $t^{1/2}$  dependence (see text).

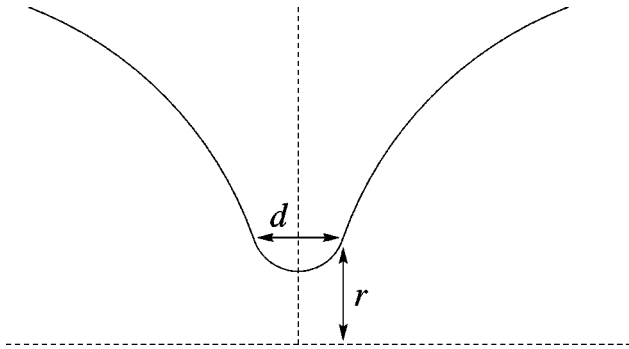


FIG. 10. Initial neck conditions for the numerical calculation.

incompressible flow is solved in a domain with moving boundaries, corresponding to the mercury phase characterized by a surface-tension coefficient of  $0.435 \text{ kg s}^{-2}$ , a dynamic viscosity of  $1.6 \times 10^{-3} \text{ kg m}^{-1} \text{ s}^{-1}$  and the already-quoted density of  $13\,600 \text{ kg m}^{-3}$ . We use a marker-and-cell method on a square grid, as discussed by Peyret and Taylor [10]. The boundary of the liquid domain is tracked by a chain of marker particles connected by third-order splines, as discussed in Refs. [11,12] so that tangents, curvatures, and their derivatives are continuous. This allows one to implement the free-surface conditions. The normal stress and tangential stress conditions on the free surface are both enforced in the method. The spline representation of the interface allows for a precise determination of the geometrical quantities such as curvature. The Navier-Stokes equation with axial symmetry is discretized on a staggered grid. Near the interface, the finite volumes are constructed out of grid cells cut by the interface. When velocities or velocity gradients are needed near the interface, extrapolations using a least-square fit to the known velocities are used. The fit is constrained by the tangential stress condition. The pressure near the interface is then given by the normal stress condition (which amounts to Laplace's law in the static case). Tests of the method on free-droplet oscillations show excellent agreement with a maximal relative error of 0.003.

In this work, the initialization of the simulation poses a peculiar problem. It is difficult to initialize a calculation with two spheres at tangency, because the singular curvature creates infinitely large capillary forces. Instead we chose to smooth the solution as shown on Fig. 10. The distances  $r$  and  $d$  are 3 and 6 grid points, respectively. This makes the initial condition dependent on the grid size so that, as the grid is refined, the solution approaches the idealized singular initial condition.

## V. COMPARISON

The results for droplet fusion are presented on Fig. 11, showing an overall qualitative agreement with the experiment (Fig. 3), and very good quantitative agreement up to the fourth frame. The differences between the experiment and the simulation may be partly explained by the fact that in the experiment the droplets are flattened by the combined effect of wetting and gravity. This introduces an energy damping, delaying the experimental motion relative to the

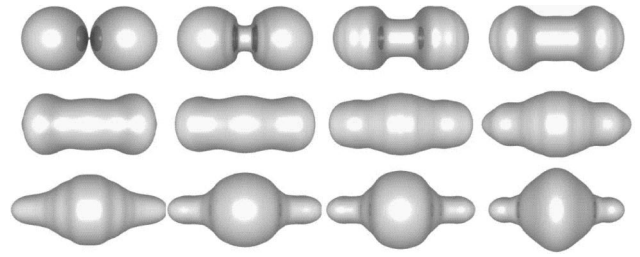


FIG. 11. Surface shape evolution predicted by numerical simulation. Time conventions as in Fig. 3.

simulation. Yet, within this limitation, we observe that both, the experiment and the simulation show the presence of capillary waves, which, emitted from the initial singularity, travel around the droplets and eventually reach the drops' far ends, creating a large localized pressure. Some experiments [13] and boundary-integral simulations [14] report the formation of a tiny jet at this point. However, either the present experimental and simulated spatial resolution are not enough to confirm the presence of such phenomenon, or the energy dissipation in our system is large enough to suppress it. In fact a significant difference between the energy dissipated near the fifth frame in the experiment, compared to the simulation, could also explain why beyond that point the simulation shows larger capillary waves than the experiment.

The simulation also allows to investigate the time evolution of the neck thickness  $R_y$ . The results are included as continuous and dashed lines in Fig. 9, corresponding to different spatial resolutions. As already mentioned, the experiment satisfies the  $t^{1/2}$  law [9] from very early times, while the simulations take some time to converge. Yet, the convergence is faster for the better grid resolution ( $1024 \times 256$ ) calculation, although it does not quite fit the experiment or the expected  $t^{1/2}$  law. It is clear that the initial shape and flow in the neck region is very poorly resolved given the small number of grid points in this area. An effect of this poor resolution is slower initial growth of the neck radius. This in

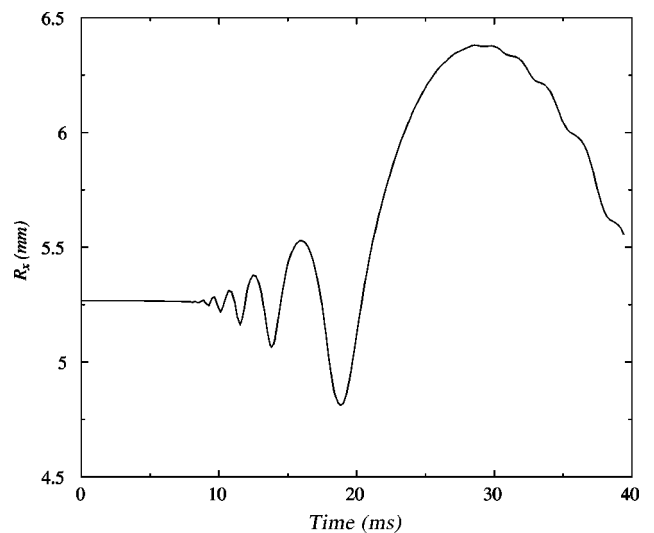


FIG. 12. Numerical estimate of the axial dimension time evolution.

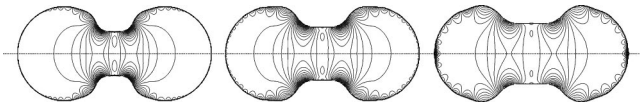


FIG. 13. Simulated pressure isolines.

turns makes apparent a relatively large transition region between the initial flat ( $t^0$ ) part and the  $t^{1/2}$  scaling. However this transition region moves to shorter times as the mesh is refined. Two effects combine to create this slower initial growth: numerical dissipation due to the coarse resolution and smaller initial impulse from surface tension due to the necessary finite initial curvature. A finer mesh is therefore needed in order to obtain a better agreement. Adaptive mesh refinement would be interesting in this respect. Still, both the data and the simulation indicate that the initial neck-growth rate is a complex function of time going from a small value in the first instants to a rapid growth ( $A \approx 0.5$ ) at intermediate times and smoothly decreasing at the later stages.

Concerning the time evolution of the axial dimension  $R_x$ , the simulation (Fig. 12) shows dramatically the arrival of the capillary waves. A similar, but less pronounced, effect is observed in the experiment (Fig. 7). Otherwise, the overall qualitative experimental features are well reproduced. Finally, as an insight into the motion dynamics of those capillary waves, in Fig. 13 we show the time evolution of the

simulated iso-pressure lines. Here we observe the propagation of the capillary waves along the surface and the formation of a large pressure point as the capillary waves reach the axis.

## VI. CONCLUSIONS

The surface-shape evolution for the coalescence of two mercury drops, driven solely by surface tension, has been studied. The use of ultrafast analog and fast-digital video cameras allowed us to observe this phenomenon on micro-second and millisecond time scales. The early formation of capillary waves originating in the contact region is reported. Those waves have an important influence on the surface-shape evolution of the coalesced drop. Numerical simulations were presented that provide a good qualitative and, to some extent, quantitative agreement with the experiment. The main differences are associated with experimental (supported liquid drops) and simulation (finite grid size) limitations. The observed neck-size evolution follows closely the  $t^{1/2}$  law predicted by Eggers, Lister, and Stone [9] for the early stages. This feature is better reproduced by the higher spatial resolution simulation.

## ACKNOWLEDGMENTS

We acknowledge the economic support of CONACYT and DGAPA-UNAM.

- 
- [1] J. Eggers, *Rev. Mod. Phys.* **69**, 865 (1997).
  - [2] W. J. Swiatecki, *Nucl. Phys. A* **376**, 275 (1982).
  - [3] M. Guilleumas, F. Gracias, M. Barranco, and E. Suraud, *Z. Phys. D: At., Mol. Clusters* **25**, 227 (1993).
  - [4] S. G. Bradley and C. D. Stow, *Proc. R. Soc. London, Ser. A* **287**, 635 (1978).
  - [5] A. Menchaca-Rocha, *J. Colloid Interface Sci.* **149**, 472 (1992).
  - [6] DALSA CA-D1-0128A Turbosensor, by Dalsa Inc.
  - [7] IMACON 792, by Hadland Photonics Ltd.
  - [8] R. Park and E. J. Crosby, *Ceram. Eng. Sci.* **20**, 39 (1965).
  - [9] J. Eggers, J. R. Lister, and H. A. Stone, *J. Fluid Mech.* **401**, 293 (1999).
  - [10] R. Peyret and T. D. Taylor, *Computational Methods for Fluid Flow* (Springer Verlag, New York, 1983).
  - [11] S. Popinet and S. Zaleski, *Int. J. Numer. Meth. Fluids* **30**, 775 (1999).
  - [12] R. Scardovelli and S. Zaleski, *Annu. Rev. Fluid Mech.* **31**, 567 (1999).
  - [13] D. Richard, Ph.D. Thesis, Université Paris VI, 2000, Fig. V.15.
  - [14] H. N. Ögüz and A. Prosperetti, *J. Fluid Mech.* **257**, 111 (1993).